AIAA JOURNAL
Vol. 34, No. 9, September 1996

Characteristic Features of Large Structures in Compressible Mixing Layers

N. L. Messersmith*
Purdue University, West Lafayette, Indiana 47907-1282
and
J. C. Dutton†
University of Illinois at Urbana–Champaign, Urbana, Illinois 61801

The large structures of compressible mixing layers have been investigated using planar laser Mie scattering visualizations from condensed ethanol droplets in the flow. Large ensembles of digital images were collected for 10 cases, corresponding to combinations of 3 distinct conditions of compressibility, 2 different image planes, and 2 seeding methods. The three flow conditions were at relative Mach numbers of 0.63, 0.98, and 1.49. The two-dimensional spatial covariance field was computed for each ensemble to characterize the typical large structure observed within the mixing layer. The spatial covariances of the transverse views indicate that the structures are elongated and compressed toward the streamline flow direction with increasing compressibility. Covariances of the oblique images help quantify the influence of compressibility on the three-dimensional nature of the structures, as evidenced by an increase in size and a reduction in eccentricity of the obliquely imaged structures with increasing compressibility.

I. Introduction

RECENT years have seen increased interest in compressible mixing layers. The emphasis of early investigations on compressible mixing layers dealt with growth rates, largely as a result of the experimentally observed reduction in growth rate of compressible mixing layers when compared with incompressible mixing layers of the same freestream velocity and density ratios.[1,2] The convective and relative Mach numbers have been found to be useful parameters for isolating the effects of compressibility from those of the velocity and density ratios in high-speed mixing layers. The definition of the convective Mach number is based upon a large structure convective velocity; however, experimental observations made by Papamoschou[3] have indicated a marked difference in the measured convective velocity from the value used in defining the convective Mach number. Furthermore, when mixing occurs between gases of different ratios of specific heats, two convective Mach numbers describe the mixing.[2] Goebel and Dutton[4] used the relative Mach number M_r as an alternative to the convective Mach number that avoids these problems and still provides a measure of compressibility in the mixing layer. The relative Mach number, which is used in this article, is defined as the freestream velocity difference normalized by the average freestream sonic velocity, $M_r = \Delta U/\bar{a}$. For mixing between gases with the same ratio of specific heats, the relative Mach number is twice the convective Mach number.

The effect of compressibility on organized structures in supersonic mixing layers has been discussed for some time. Many early flow visualizations using schlieren or shadowgraph photography did not clearly show the classic, two-dimensional large structures typically observed in incompressible mixing layers.[5] This is probably because of the spanwise integrating nature of these techniques; however, indirect evidence of the presence of large-scale turbulent structure was observed. More recent schlieren studies[2,6,7] of compressible mixing layers have achieved varying success in imaging large turbulent structures. A number of the visualizations exhibit a braided appearance in the mixing layer, much like that seen in incompressible mixing layers, but not as clearly defined.

Planar imaging techniques afford tremendous improvements in the spatial resolution of large-scale inviscid structures and have been successfully employed in the compressible mixing layer.[8–13] Clemens and Mungal[10] used both scalar transport and product formation seeding of condensed ethanol (see also Clemens and Mungal[14]), and their Mie scattering images provide evidence of the existence of large-scale structures in compressible mixing layers at relative Mach numbers up to 1.53. The large structures they observed were most clear and coherent in low compressibility flows, and plan views indicate that these structures are generally two dimensional in the spanwise sense. The descriptor coherent is used here to suggest Brown and Roshko[5]-type, two-dimensional, spanwise rollers. As the compressibility of the mixing layer increases, plan views show a disintegration of the spanwise organization of the structure, first by skewing of the structures, followed by a nearly complete breakdown in two-dimensional organization. These trends were also observed by Elliott et al.[11] and Samimy et al.,[15] using both filtered Rayleigh scattering imaging and pressure correlation measurements. The skewing and breakdown of the spanwise structures are likely reasons for the shortcomings of schlieren photography in imaging large structures under compressible conditions.

Three-dimensional stability analyses have also predicted trends of this nature.[16–19] Sandham and Reynolds,[16,17] Soetrisno et al.,[18] and Soetrisno[19] found that the spanwise organization of a large structure is primarily two dimensional up to relative Mach numbers of around 1.2. However, three-dimensional structures can still be found for $M_r < 1.2$. Indeed, significant changes in the structure topology can be induced by the crossing of oblique Kelvin–Helmholtz instabilities even at low levels of compressibility.[19] As the relative Mach number increases above 1.2, three-dimensional instability modes grow at the same rate as the two-dimensional modes, producing a quasitransition region in which the spanwise structures begin to skew obliquely to the flow and eventually break up. Above a relative Mach number near 2.0, Sandham and Reynolds[17] predict the mixing layer structure to be essentially three dimensional.

Other studies[8–11] have obtained images of compressible mixing layer structures; however, these investigations have not presented a characteristic or typical structure based upon ensemble statistics. The work of Clemens and Mungal[10] employed a similar seeding technique as the present investigation for approximately the same range of compressibility in a supersonic mixing layer. In their work, they proposed that the nature of the large structure changes from an elliptical shape at low compressibility to a more polygonal shape with increasing compressibility. A kink is also noted as developing in

Received Feb. 28, 1995; revision received Jan. 30, 1996; accepted for publication Feb. 17, 1996.

*Assistant Professor, School of Aeronautics and Astronautics. Member AIAA.
†Professor, Department of Mechanical and Industrial Engineering. Associate Fellow AIAA.

the braid region with increasing compressibility. Inspection of their images does indeed show clear examples to support their conclusions, although further inspection of the same images also illustrates the presence of a wide variety of structures (at all levels of compressibility), both elliptical and polygonal shaped large structures with and without the kink in the braid region. This variety of structures contained in instantaneous images highlights the difficulty of visually identifying typical structures at any flow condition.

In an effort to minimize subjectiveness, the present investigation has placed particular emphasis upon the statistical characterization of the structures observed in compressible mixing layers. Ensembles of 256 digital images are analyzed for the two-dimensional spatial covariance fields to identify the characteristic large-scale structures. Understanding is sought as to the effect of compressibility on the mixing layer structural features. Three distinct flow conditions were considered, with relative Mach numbers of 0.63, 0.98, and 1.49. Mie scattering from condensed ethanol droplets was performed for all of the cases. Two types of seeding techniques were employed: scalar transport and product formation (the same as used by Clemens and Mungal[14]). For scalar transport seeding, ethanol was injected into one of the streams upstream of the plenum chambers. Condensation of the ethanol vapor in the nozzle produced a fine dispersion of droplets in the supersonic freestream. The product formation technique involves seeding ethanol vapor into a subsonic flow, with the droplets formed by a condensation reaction initiated by the mixing of the vapor-laden subsonic stream with a cold supersonic stream. Two image planes were viewed: transverse and oblique. The transverse image plane (side view) was used to establish the large structure sizes and orientations. The oblique image plane was used to observe the spanwise structure and to highlight the three-dimensionality of the mixing layer.

II. Experimental Apparatus

The experiments were conducted in a dual-stream supersonic mixing layer wind tunnel at the University of Illinois at Urbana–Champaign.[4,6,13,20] The facility is shown schematically in Fig. 1. Two supersonic half-nozzles (Mach 1.38 and 2.45) are separated by a thin splitter plate, with the height of each incoming stream being 23.5 mm. The half-nozzles were designed using a method of characteristics code combined with a compressible boundary-layer code to account for viscous effects in the diverging section of the nozzle and along the splitter plate. The splitter plate converges the two streams at 2.5 deg and has a tip thickness of 0.5 mm. The test section is 95 mm wide, 47.5 mm high, and nearly 500 mm long. The upper and lower walls of the test section are adjustable, so that a neutral pressure gradient can be established in the test section. Fused silica windows are installed in the side walls for image collection and permit half of the test section length to be viewed at any one time. Also, narrow fused silica windows are mounted in the top and bottom walls for laser sheet access. The separate plenum conditions for the two streams are independently controlled, and flow conditioning (two screens, a honeycomb and a final screen) occurs before the flow enters the nozzle contractions.

During the experiments, liquid ethanol was injected through an atomization nozzle roughly 5 m upstream of the test section to ensure complete evaporation and mixing of the vapor with the carrier air before expansion through the nozzles. Ethanol mass fractions were 0.5% of the carrier air for the scalar transport experiments, whereas the product formation studies required seeding at 2% mass fraction for a reasonable signal strength. Despite the increase in the seeded ethanol mass fraction, the product formation images were of much lower signal intensity ($S/N \approx 4$–6) than the scalar transport images ($S/N \approx 30$–50), as a result of the dilution of the ethanol vapor concentration within the mixing layer in the product formation experiments. In the scalar transport seeding cases, the freestream seeding was very uniform and quite repeatable, with standard deviations of the freestream scattering intensity typically below 2%.

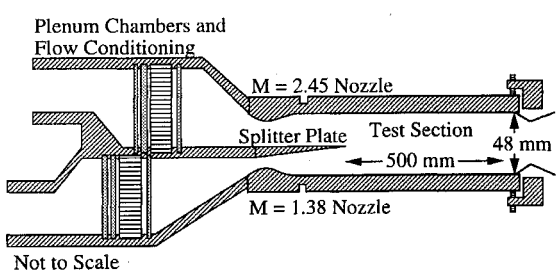

Fig. 1 Schematic of supersonic mixing layer facility.

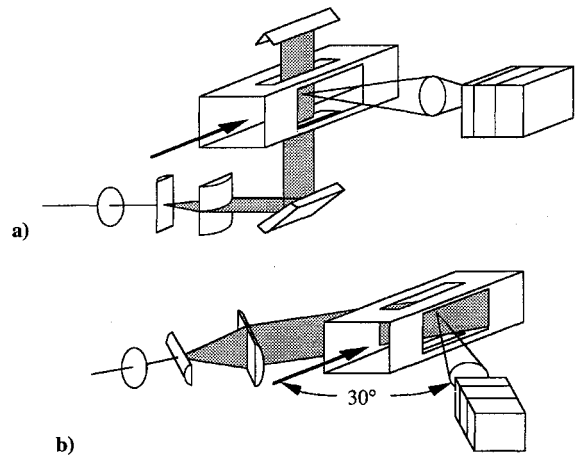

Fig. 2 Schematic of a) transverse and b) oblique image planes.

Figure 2 illustrates the difference between the transverse and oblique image planes. In both image arrangements the camera is perpendicular to the laser sheet. The transverse plane is a standard side view, whereas the camera position for the oblique images was at an angle of 30 deg to the streamwise flow direction with the laser sheet being at 60 deg to the streamwise direction. The physical construction of the wind tunnel prohibited imaging the ideal spanwise cross-sectional view (end view with the laser sheet perpendicular to the flow direction). The 60-deg angle of the laser sheet was used for the oblique image plane since it provided the greatest possible spanwise field of view in the facility, 24 mm in the spanwise direction. Because of internal reflections of the laser sheet from the ground glass edges of the wind-tunnel window, it was necessary to center the oblique images further downstream than the transverse images so that the laser beam was dumped into the test section side wall. As a result, the transverse images were centered 190 mm from the tip of the splitter plate, whereas the oblique images were centered 240 mm from the splitter plate tip.

The image acquisition system was based on a Questek 2420 XeCl excimer laser. The pulse duration was 15 ns, with pulse energies adjustable from 100 to 200 mJ. Using appropriate optics, the laser beam was fashioned into a sheet 50 mm wide by 0.3 mm thick. Images were collected using a microcomputer-based image processing system interfaced to a 12-bit, intensified Reticon 128 × 128 photodiode array camera. A UV-Nikkor 105 mm/ƒ4.5 ultraviolet lens was used to collect the scattered light. For all of the cases studied, the camera magnification was 0.4, resulting in an imaged flow area 32 mm square. Masking of edge effects of the camera reduced the effective field of view to 26 mm horizontally by 30 mm vertically. Before each ensemble of images was analyzed, postprocessing of the raw data was performed. First the camera dark current and background were subtracted from each image. The resulting images were then normalized with an image that corrected for the average spatial variation of the laser sheet intensity convoluted with the spatial variation of the camera pixel sensitivities (intensifier photocathode responsivity). The normalization image was obtained with a fine dispersion of smoke particles injected into the test section. Further details concerning the overall design of the wind-tunnel facility as well as specific details of the diagnostics employed in this study can be found in Messersmith.[13]

III. Results

A. Experimental Conditions

Three different flow conditions were examined, with relative Mach numbers of 0.63, 0.98, and 1.49. The experimental operating

conditions for each flow are compiled in Table 1. Wall static pressure, plenum stagnation pressure, and stagnation temperature measurements were used to determine the flow conditions, which were quite stable, as indicated by the uncertainty estimates also listed in Table 1. Flow 1 ($M_r = 0.63$) represents the mixing between Mach 2.45 and Mach 1.38 streams. Flow 2 ($M_r = 0.98$) is the mixing between Mach 1.38 and Mach 0.27 streams, with the Mach 0.27 stream created by operating the Mach 2.45 nozzle unstarted. Flow 3 ($M_r = 1.49$) is the mixing between Mach 2.45 and Mach 0.43 streams, with the Mach 0.43 stream created by operating the Mach 1.38 nozzle unstarted. The mixing layer thickness b is based upon the average Mie scattering intensity profile and is found using the 10% cutoff from each freestream scattering intensity value, in a manner analogous to that used by Goebel and Dutton[4] for velocity measurements. This thickness is also used to estimate the local mixing layer Reynolds numbers Re_b. Each case is composed of an ensemble of 256 images. Table 2 lists the results of the covariance analysis to be discussed later. The shorthand names for the cases considered can be summarized as C#OT (or B, P), where # is the flow condition, T is top stream scalar transport seeding, B is bottom stream scalar transport seeding, and P is product formation seeding. The O indicates the oblique image plane.

B. Individual Images

The images shown here are presented such that the flow is from left to right. The seeded fluid is light and the unseeded fluid is dark. Furthermore, as indicated in each of the photographs and spatial covariances to follow, the physical scale is 26 × 26 mm. In the transverse image plane, the horizontal and vertical directions in the images represent the streamwise and transverse directions of the flow, respectively. The flow structures imaged in the transverse plane are most characteristic of the predominant, two-dimensional spanwise structure in the mixing layer. The geometry is more complicated in the oblique image plane. The oblique view images a width of roughly two mixing layer thicknesses and as such is used to capture the three-dimensional nature of the mixing layer. The present work is directed at the large-scale flow structures, which often are observed to extend across the entire mixing layer.

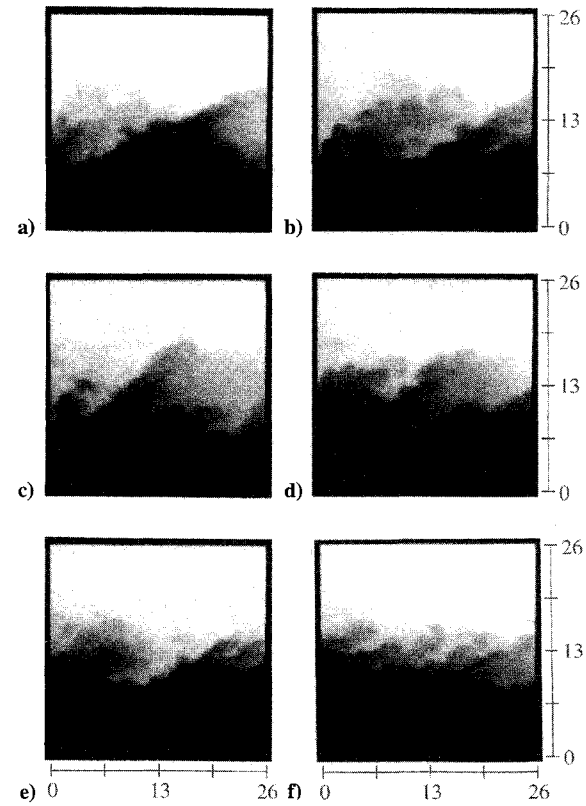

Fig. 3 Representative instantaneous images from case C1T. Dimensions in millimeters.

Table 1 Experimental conditions

Quantity	Flow 1	Flow 2	Flow 3	Uncertainties, %
M_r	0.63	0.98	1.49	1.0
$r = U_2/U_1$	0.71	0.23	0.25	2.0
$s = \rho_2/\rho_1$	0.63	0.73	0.47	0.6
M_1	2.45	1.38	2.45	0.1
M_2	1.38	0.27	0.43	1.9
P_{t1}, kPa	727	183	569	0.2
P_{t2}, kPa	142	62	41	1.1
P_{static}, kPa	46	59	36	1.6
T_{t1}, K	279	285	279	0.4
T_{t2}, K	279	285	279	0.4
ΔU, m/s	160	306	412	1.2
b, mm	11.2	9.8	12.5	2.3
$Re/1, 10^6$/m	13.5	16.3	17.8	1.2
$Re_b, 10^5$	1.5	1.6	2.3	2.4

Table 2 Characteristics of the two-dimensional spatial covariance fields

Case	Image[a]/seed[b]	Size[c]	Eccentricity[d]	Angle, deg
C1T	T/S	0.69 ± 0.03	0.52 ± 0.04	26 ± 2
C1B	T/S	0.69 ± 0.03	0.52 ± 0.04	27 ± 2
C2B	T/S	0.85 ± 0.03	0.45 ± 0.03	25 ± 2
C3T	T/S	1.03 ± 0.03	0.58 ± 0.02	16 ± 1
C3P	T/P	0.66 ± 0.02	0.48 ± 0.03	—
C1OT	O/S	0.48 ± 0.03	0.30 ± 0.06	—
C1OB	O/S	0.53 ± 0.03	0.36 ± 0.05	—
C2OB	O/S	0.77 ± 0.03	0.14 ± 0.04	—
C3OT	O/S	0.71 ± 0.03	0.10 ± 0.04	—
C3OP	O/P	0.75 ± 0.03	0.34 ± 0.03	—

[a]T = transverse, O = oblique.
[b]S = scalar transport, P = product formation.
[c]Dimensionless structure size defined as major axis of 50% correlation contour divided by the local mixing layer thickness.
[d]Eccentricity defined as unity minus the ratio of minor axis to major axis of the 50% correlation contour.

It has been stressed earlier that a rich variety of flow structures is observed in all cases; however, space limitations preclude extensive photographic reproduction. To help illustrate the motivation for the statistically based covariance analysis, though, a number of images are reproduced in Fig. 3 for case C1T ($M_r = 0.63$). Figures 3a–3e contain realizations of structures suggestive of large-scale rollers (Brown–Roshko type[5]), whereas Figs. 3c–3f also exhibit substantial smaller scale structure. The distinction of smaller scale structures used here is any form with a transverse extent that is not as large as the largest vortex rollers, without specific regard to the shape of the small structure. Such small scales are highlighted in Fig. 3f, which appears devoid of the largest structures found in the other figures and yet possesses a variety of small, elongated structures separated by thin filaments of high-intensity fluid (braids). With respect to the shape of the largest structures at this low compressibility condition, the large structure captured in Fig. 3c has a particularly striking resemblance to the type of polygonal structure noted by Clemens and Mungal[10] to occur at much higher levels of compressibility. Reiterating, this variability is found in all ensembles in the present investigation and is also found in the work of Clemens,[8] Clemens and Mungal,[9,10] and Elliott et al.,[11] reinforcing the necessity for a statistical measure to characterize the typical large structure of each ensemble.

Selected images from the transverse imaging of cases C1B, C2B, and C3T are collected in Fig. 4. Case C1B, Figs. 4a and 4b, is identical to C1T, except for the seeding arrangement. Many of the large structures observed in the low compressibility condition in flow 1 (both cases C1T in Fig. 3 and C1B in Figs. 4a and 4b) appear well organized and similar to those seen in incompressible mixing layers.[5,21] The orientation of the structures appears reversed for the case C2B ($M_r = 0.98$) images, Figs. 4c and 4d, since the bottom stream (seeded) is now the high-speed stream. The images suggest considerably more shearing or tearing of smaller scale filaments from the larger structures than seen in the lower compressibility

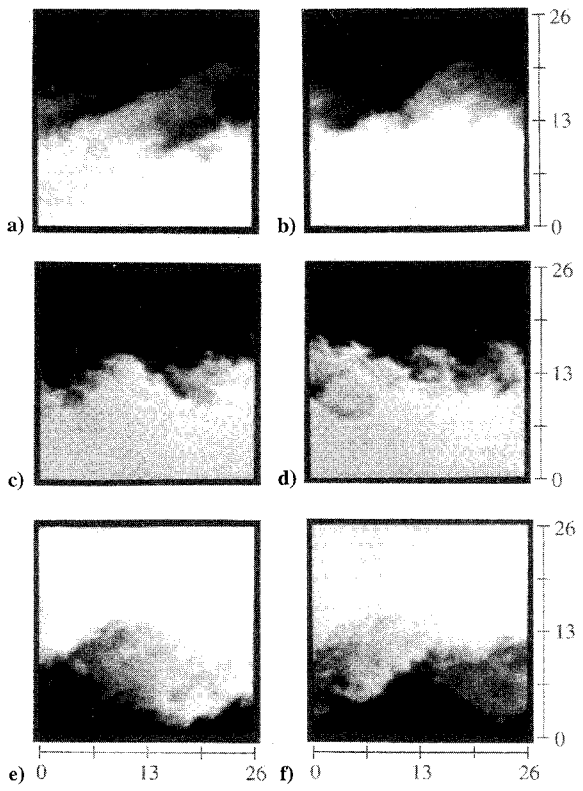

Fig. 4 Representative instantaneous images from transverse imaging cases: a) and b) C1B, c) and d) C2B, and e) and f) C3T. Dimensions in millimeters.

case. Also apparent for this case is the relative lack of intermediate scattering intensities (gray scales), which indicates a lack of mixing that has been confirmed with measurements of the scalar probability density function.[13,22,23] At the highest level of compressibility studied, the case C3T ($M_r = 1.49$) images, Figs. 4e and 4f, capture large structures with a smoother appearance reminiscent of those seen in flow 1. Small-scale intrusions into the large structures seem more common, and a wider range of scales is present in the flow 3 structures compared with flow 1. The stringy filament structures observed with great regularity in flow 2 are also imaged in flow 3, but the overall structures at the high compressibility level of flow 3 are not as distorted as in the intermediate compressibility case of flow 2. Although not specifically discussed by Clemens and Mungal,[10] their results do illustrate the same general trends found here. In particular, there is a lack of intermediate intensity values with a noticeable occurrence of stringy filament type structures at their intermediate compressibility case ($M_c = 0.5$). These filament structures are not as prevalent in either the lower or higher compressibility cases studied, and for these cases a much fuller range of intermediate scattering intensities is readily observed. Clemens and Mungal[10] identify this intermediate compressibility case as the transitional condition where the polygonal structures and kinked braids begin to appear.

Figure 5 includes a compilation of instantaneous images from the oblique view. In the oblique plane, what appears to be a large structure is occasionally captured; however, the majority of structures imaged are smaller in scale than their transverse plane counterparts found in Figs. 3 and 4. Often observed are structures with a form (mushroom shaped) that suggests that a pair of counter-rotating vortices have been imaged. Although it cannot be unequivocally determined that the flow phenomenon producing these structures is indeed a pair of counter-rotating vortices, the presence of a vortex pair would serve to entrain fluid through the space between the vortices, thereby resulting in the mushroom shaped appearance when imaged. Such vortex pairs have been clearly imaged before by Bernal and Roshko[21] in liquid mixing layers and can be seen in the more recent images by Clemens and Mungal[10] in supersonic mixing layers. Thus, the mushroom shape is assumed to be associated with a jet of fluid induced by the presence of a counter-rotating

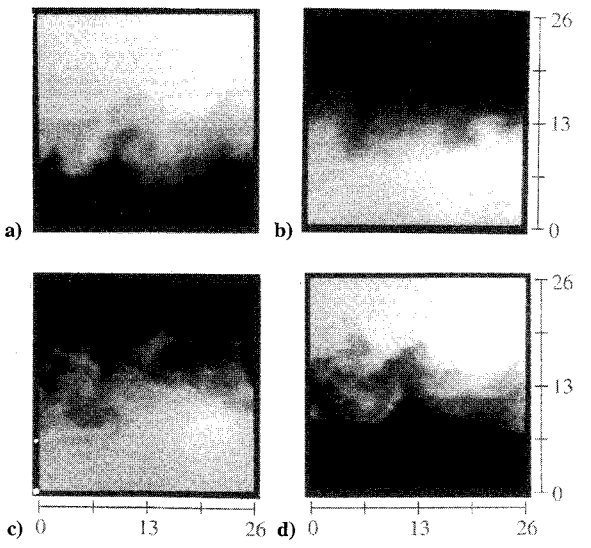

Fig. 5 Representative instantaneous images from oblique imaging cases: a) C1OT, b) C1OB, c) C2OB, and d) C3OT. Dimensions in millimeters.

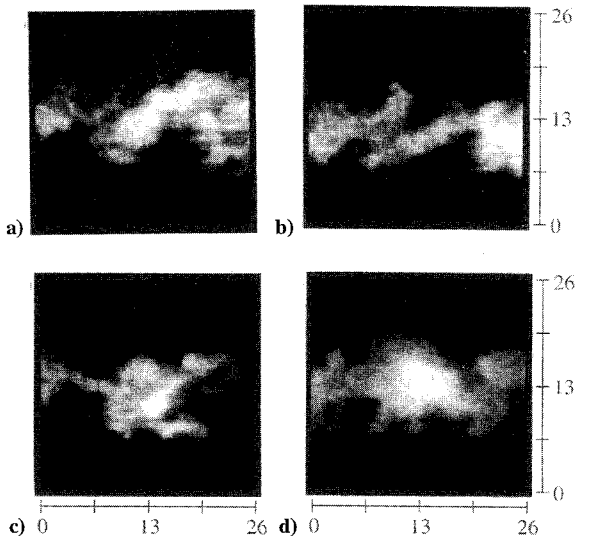

Fig. 6 Representative instantaneous images from product formation seeding cases: a) and b) C3P (transverse view) and c) and d) C3OP (oblique view). Dimensions in millimeters.

vortex pair. Such a jet of fluid entrained from one freestream is often observed adjacent to a jet of fluid entrained from the opposite freestream, thereby giving the appearance of an undulating mixing layer shape. Furthermore, such counter-rotating vortices are known to be generally aligned in the streamwise direction and smaller in scale than the underlying large-scale spanwise structure.[21] Distinct realizations of these entrained fluid jets can be seen as entrainment of unseeded (dark) fluid in the center of Fig. 5a (case C1OT), as a pair (one light, one dark) in the right half of the mixing layer in Fig. 5b (case C1OB), as entrainment of unseeded fluid in the left central portion of the mixing layer in Fig. 5c (case C2OB), and as multiple interacting jets in the left half of Fig. 5d (case C3OT).

Seeding of the subsonic stream in flow 3 permits the imaging of ethanol product formation, cases C3P and C3OP. Representative images are shown in Fig. 6. The signal-to-noise ratio in these images ($S/N \approx 4-6$) is substantially lower than for the scalar transport images ($S/N \approx 30-50$). The oblique product formation images have a halo because of background correction difficulties associated with the internal reflections caused by dumping the laser sheet into the side wall; nevertheless, the key features of the flow are still visible. In general, the large structures are the high signal pockets of mixed fluid and are clearly visualized in both the transverse and oblique

image planes. The higher scattering intensity at these locations is a result of larger droplets, which are formed in the structures well upstream of the viewing station and continue to grow as the structure entrains additional ethanol vapor during convection downstream. In contrast, droplets formed in the diffusion layer of the strained interface are only recently nucleated, do not have sufficient time to grow larger than the very small initial nucleation size, and therefore exhibit a lower scattering signal. Despite the lower signals, significant amounts of product are imaged within the braid regions, suggesting that the time scales of nucleation and condensation are fast with respect to the fluid dynamic time scales.[23] In particular, many product formation images from both the transverse and oblique planes suggest that the undulating nature of the mixing region is the result of vortex interactions inducing entrainment (mushroom-shaped jets) from both freestreams into the shear layer. As discussed earlier in relation to the scalar transport seeded oblique images, it is assumed that the vorticity generating these flow structures is predominantly oriented in the streamwise direction.

C. Spatial Covariance Analysis

Given the wide variety of structures observed in an ensemble, the characterization of the predominant size, shape, and orientation of mixing layer structures as a function of the flow conditions requires the use of an objective, statistically based analysis. In this study the two-dimensional spatial covariance was used. By extension to a two-dimensional format from the one-dimensional covariance field used by Long et al.,[24] the spatial covariance field of an ensemble, $C(\Delta i, \Delta j)$, is formed from the sum of N individual image covariances, $C_n(\Delta i, \Delta j)$, using

$$C(\Delta i, \Delta j) = \frac{1}{N} \sum_{n=1}^{N} C_n(\Delta i, \Delta j) \tag{1}$$

where

$$C_n(\Delta i, \Delta j) = \frac{1}{R^*} \sum_{m=1}^{R^*} I'(i, j) I'(i_m^*, j_m^*) \tag{2}$$

For each image, the difference in the pixel intensity from the ensemble mean pixel intensity is used, $I'(i, j) = I(i, j) - \bar{I}(i, j)$, hereafter referred to as the intensity fluctuation. The pixel lag parameters Δi and Δj are given by $\Delta i = i - i^*$ and $\Delta j = j - j^*$, respectively, where the pixel (i^*, j^*) is the reference point about which the other image pixels are correlated. The conversion from pixel lag size to physical dimensions is accomplished with the aid of the known image magnification and detector size. Each individual image covariance C_n contains the superposition of many reference points R^* that contribute to the total correlation at the given lag values $(\Delta i, \Delta j)$. Lag parameters span the dimension of the digital image (128 × 128) about the central $(\Delta i, \Delta j) = (0, 0)$ point (i.e., $-127 \leq \Delta i \leq 127$ and $-127 \leq \Delta j \leq 127$).

Before describing the choice of reference points used, it is instructive to illustrate the meaning of the spatial covariance. For the present application, where the Mie scattering intensity is proportional to the local fluid mixture fraction (1.0 for seeded fluid and 0.0 for unseeded fluid), a negative intensity fluctuation indicates fluid more closely related to the unseeded freestream, whereas positive intensity fluctuations are related to the seeded freestream fluid. The covariance can have values from −1 to 1 (Ref. 25), with a value of 1 indicating perfect correlation and a value of 0 indicating no correlation [between two points (i, j) and (i^*, j^*)]. As expected with a noisy signal,[25] perfect negative correlations (covariance of −1) are not obtained in any cases of the present study. Inspection of Eqs. (1) and (2) clearly shows that positive correlation will occur when both interrogation points possess intensity fluctuations of the same sign. Thus, the spatial covariance registers the spatial extent (in all directions) over which the fluid is related to the fluid at the reference point, with the value of the covariance being a measure of the relative strength of the correlation. As is typically done with the autocorrelation, the covariance is normalized to unity for zero lag values, since any parcel of fluid is always perfectly correlated to itself.

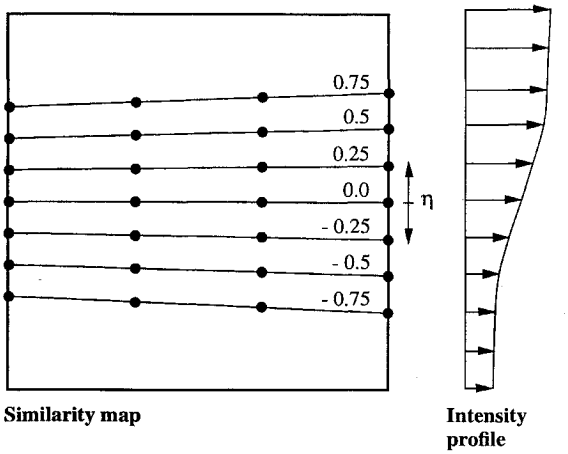

Fig. 7 Sampling grid for computation of spatial covariance field.

Since all points in an image are potential reference points, the influence of the chosen reference point(s) must be considered. If all of the pixels in an image are used as reference points, the summations given by Eqs. (1) and (2) result in the two-dimensional spatial autocorrelation.[25] This procedure was initially applied to the current images; however, it was found that the autocorrelation image did not yield clear information concerning mixing layer structures. This arose as a result of the smoothing influence of large regions of uncorrelated freestream fluid. The autocorrelation was then performed over only the central 64 rows (16 mm) that spanned the extent of the mixing layer. This avoided large regions of uncorrelated freestream fluid and provided correlation contours related to the large structure size. However, information regarding the angular orientation of the large structures, evident in the instantaneous images, was lacking. At the opposite end of the spectrum from the autocorrelation is the covariance field based upon only a single reference pixel per image. Smoothing still arises in this technique as well, albeit to a limited extent, since the reference point might lie inside a structure in many frames but outside in many other frames of the ensemble.

To enhance the probability that several reference points would be located within a large structure (in every image), a grid of reference points was generated. The grid was centered on the mixing layer, thereby excluding the majority of the freestream pixels. The grid was established utilizing a similarity map for each ensemble that provides, from case to case, similar locations of sampling points. Figure 7 illustrates how the grid of sampling locations, based upon a transverse similarity variable $\eta = (y - y_0)/b$, was chosen from the mean intensity profile of each image ensemble, where y_0 is the location at which the mean intensity is the average of the freestream intensities. The reference points chosen coincided with lines of constant transverse similarity coordinate set at $\eta = -0.75, -0.5, -0.25, 0, 0.25, 0.5$, and 0.75, which provided coverage of the mixing layer core ($-0.5 \leq \eta \leq 0.5$) as well as regions of large-scale intermittency ($\eta = \pm 0.75$) and yet eliminated the great majority of the uncorrelated freestream pixels. Four columns evenly spaced streamwise across the image complete the grid, resulting in 28 reference points per image. The covariance results presented next were invariant when the grid was reduced by 30% (by eliminating the $\eta = \pm 0.75$ reference points).

For each of the covariances presented next, the contour lines are in even increments of 0.125 about the central peak, which is normalized to 1.0. The contour for 0.0 is not shown to avoid undue noise from the uncorrelated freestreams. Also, the 0.5 (or 50%) correlation contour level is used to quantify the large structure size and orientation as compiled in Table 2. For scaling purposes, the frame around each covariance field is the size of an individual image, allowing correlations up to ±13 mm in either direction from the central peak. The ensemble-averaged spatial covariance highlights an elliptically shaped, typical large structure with the major axis inclined to the streamwise flow direction. Basing the characterization of the large structure upon an ellipse, Table 2 lists the dimensionless structure

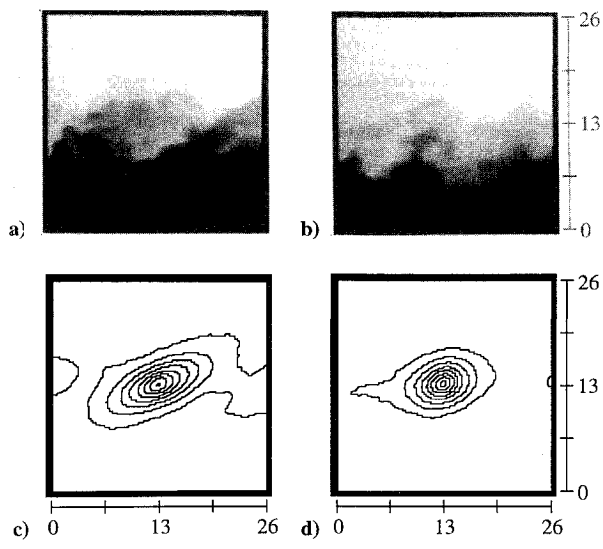

Fig. 8 Comparison of an instantaneous image of cases a) C1T and b) C1OT to the spatial covariance field of cases c) C1T and d) C1OT. Dimensions in millimeters.

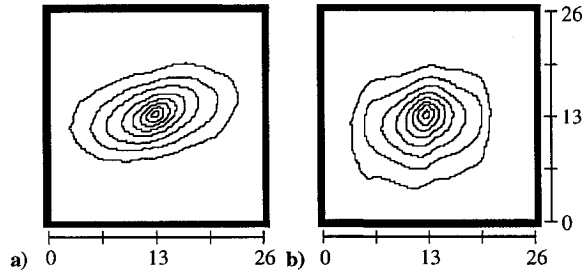

Fig. 9 Spatial covariance fields of cases a) C2B and b) C2OB. Dimensions in millimeters.

size (ratio of major axis to mixing layer thickness), ellipse eccentricity (unity minus the ratio of minor axis to major axis), and angular orientation of the major axis. The angular orientation of the structures is with respect to the horizontal direction of the image plane, which in the transverse images corresponds with the streamwise flow direction.

It is unreasonable to expect that the ensemble-averaged covariance will identify a typical mixing layer structure that will appear precisely like any of the large structures found in a given instantaneous image. Nevertheless, the comparison of instantaneous images and spatial covariances of both the transverse case C1T and the oblique case C1OT shown in Fig. 8 reveals a great similarity, especially in the transverse results. The spatial covariance results for cases C1B and C1OB are nearly identical to cases C1T and C1OT and are itemized in Table 2, although the covariance fields are not shown. The good agreement in the correlated structure size, shape, and orientation between these two cases, both for the transverse and oblique views, indicates independence of the results from facility or seeding effects. For this low compressibility flow 1, the transverse plane structures are inclined to the horizontal (streamwise) direction at roughly 26 deg. With respect to the mixing layer thickness, the 50% correlation contour yields a dimensionless structure size of 0.69 and an eccentricity of 0.52.

The transverse structures in case C2B, shown in Fig. 9 along with the covariance from case C2OB, are larger with a dimensionless structure size of 0.85, yet slightly less eccentric (0.45 compared with 0.52), than those in flow 1. There is also only a slight change of the angular orientation toward the horizontal from 26 to 25 deg. For flow 3, the transverse structures can be seen to stretch and align themselves more toward the horizontal axis, as shown in Fig. 10a for case C3T, along with the results for the oblique case C3OT in Fig. 10b. At these flow conditions, the structures viewed in the

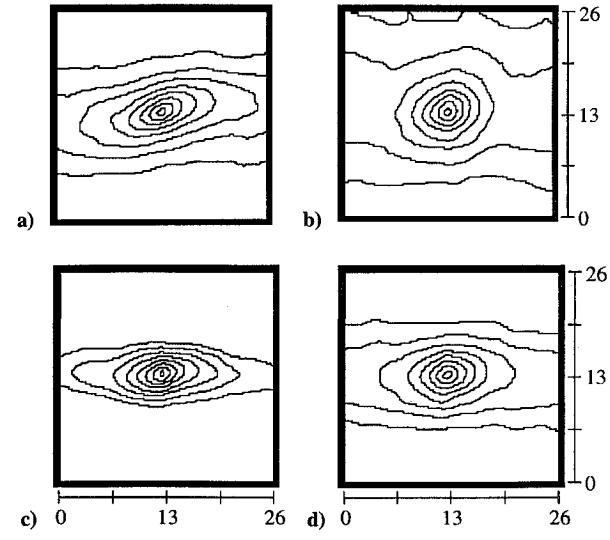

Fig. 10 Spatial covariance fields of cases a) C3T, b) C3OT, c) C3P, and d) C3OP. Dimensions in millimeters.

transverse plane have a larger dimensionless structure size of 1.03 and an eccentricity of 0.58, and the angular orientation has dipped to roughly 16 deg from the horizontal. The covariance results of case C3P and C3OP (Figs. 10c and 10d, respectively) exhibit a transverse structure dimensionless size and eccentricity of 0.66 and 0.48, respectively. The angular orientation of case C3P is omitted from Table 2, since the product formed in the braiding region will lead to a correlation biased along the streamwise flow direction.

Dimensionless structure sizes and eccentricities derived from the covariance analyses of the oblique views are given in the lower portion of Table 2. Angular orientations are not included for these views since the complicated image plane geometry for these more rounded structures renders it difficult to determine a dominant angle.

IV. Discussion

The covariance results presented in Table 2 reveal some clear trends regarding the large-scale structures in compressible mixing layers. Attention will be focused initially in this discussion on the scalar transport seeded cases, whereas the product formation cases will be discussed later.

In the transverse image plane the large-scale structures increase in dimensionless size with increasing compressibility. Comparison of flow 1 ($M_r = 0.63$) with flow 2 ($M_r = 0.98$) shows an increase in the transverse structure size of 23% for flow 2. Likewise, comparing flow 1 with flow 3 ($M_r = 1.49$), the transverse structure is larger by 49% for flow 3. However, since Elliott at al.,[11] Samimy et al.,[15] and Clemens and Mungal[10] have presented significant experimental results illustrating the sweep of large structures with increasing compressibility, it is known that some of the observed size increase in flow 3 can be attributed to the altered geometric projection of a swept two-dimensional, large-scale structure. Using the relationship developed from linear stability theory to correct for the sweep of large structures, $M_r \cos\theta = 1.2$ (Refs. 16–19), the 49% increase in dimensionless structure size from $M_r = 0.63$ to 1.49 is reduced to roughly 20%. This correction yields a large structure size (0.83) for the high compressibility case, $M_r = 1.49$, that is essentially the same as for the intermediate compressibility case, $M_r = 0.98$. The large structures at the intermediate flow condition are not corrected for sweep, since stability theory does not predict skewing at this level of compressibility.

As the level of compressibility is increased, the eccentricity of the structures viewed in the transverse plane remains relatively constant at approximately 0.52 ± 0.07. On the other hand, the angular orientation of the transverse structures to the streamwise direction decreases sharply from the values for flows 1 and 2, which are 26 and 25 deg, respectively, to about 16 deg for the high compressibility case of flow 3. Thus, over the range of parameters investigated here, the effects of increasing compressibility are that the elliptically

shaped transverse structures are larger in a dimensionless sense, are oriented more toward the flow direction, and are of relatively constant eccentricity.

The effects of compressibility on the structures viewed in the oblique plane are shown by the covariance results in the bottom portion of Table 2. For flow 1 (cases C1OT and C1OB) the nondimensional structure size is about 0.5, whereas for the two higher compressibility cases, C2OB and C3OT, the size increases to about 0.75. The oblique structure dimensionless size for flow 3 is slightly smaller than for flow 2, 0.71 vs 0.77; however, the question of whether the oblique structure size will be even smaller at higher compressibility levels than those studied here must be answered by future investigations. What is clear from the current study is that the oblique structures for the two more compressible cases are definitely larger than for the low compressibility case. The covariance analysis also shows a more pronounced growth in the oblique structures than in the transverse structures with increased compressibility. In particular, the increase in the oblique structure size is approximately twice the increase in the transverse structure size (corrected for sweep) from $M_r = 0.63$ to 1.49.

In discussing the increased size of both the transverse and oblique structures with increased compressibility, the possible effects of Reynolds number should be noted. Flow 2 represents an increase in the relative Mach number of 56% with very little change in the local Reynolds number Re_b as compared with flow 1 (see Table 1). Thus, any effects noted between flows 1 and 2 are a result of compressibility. However, for flow 3, the relative Mach number increases by 137% and the local Reynolds number increases by 53% as compared with flow 1. In this latter comparison, even though both M_r and Re_b increase, the change in compressibility is believed to be primarily responsible for the noted increases in both the transverse and oblique structure sizes. This is a result of the large change in M_r in this case (137%), which occurs over the range with the greatest change in the normalized mixing layer growth rate.[2,4] The local Reynolds number, however, increases more modestly (53%), and all values are in the region of fully developed mixing.[4,6] Thus, the influence of Reynolds number is expected to be minimal and the increased transverse and oblique structure sizes measured with the covariance analysis are attributed to increased compressibility.

In addition to increased size, the covariance analysis shows that the oblique structure eccentricity decreases strongly with increasing compressibility (Table 2). This is a result of the more extensive three-dimensionality of the structures (greater randomness of orientation and size, hence reduced correlation) observed in the mixing layer from the oblique perspective. The present results indicate that increasing compressibility leads to increased size and influence of three-dimensional structures in the mixing layer. Such an increase in three-dimensionality will significantly influence the interfacial surface area and mixing rates.

Comparison of the size and eccentricity between the transverse and oblique views at the same compressibility level shows that, in every case, the oblique structures are smaller and have lower eccentricity than their transverse counterparts. The three-dimensionality observed in the oblique plane (considerable random orientation of structures) results in both a reduced correlation distance and a loss of angular information. This lack of angular information, in turn, reduces the covariance eccentricity. The result is a more rounded oblique structure with a smaller dimensionless size ratio.

The relative similarity of the statistical covariance results (Table 2) for the structure size of product formation cases C3P and C3OP also indicates the strong three-dimensionality of the mixing layer under compressible conditions. In the product formation seeding technique, ethanol only condenses in the mixing layer, and scattering only occurs from those structures containing condensed drops. If the structure was a well-defined two-dimensional spanwise roller, the oblique images would reveal an increased dimensionless size, but with an eccentricity that approached unity. If, on the other hand, the structure has begun to lose its spanwise organization, the two different image planes may not necessarily yield very different covariances, since the orientation of the structure as it passes the image plane possesses less spanwise organization. Thus, the similar covariance results for the structure size in the transverse and oblique image planes of product formation cases C3P and C3OP suggest that these structures have indeed lost organization in the spanwise dimension. On the other hand, despite this evidence of strong three-dimensionality, the differences between the transverse and oblique image planes (at a given condition) for the scalar transport seeded cases suggest that some remnant of spanwise two-dimensionality still exists over the range of relative Mach numbers studied. Unfortunately, the spatially correlated extent of the spanwise dimension could not be determined from the present measurements.

Comparison of the covariance analysis to previous results can only be addressed in a qualitative manner, since Clemens,[8] Clemens and Mungal[9,10] and Elliot et al.[11] did not subject their imaging results to statistical analysis. The increase in dimensionless size and reduction in angle under compressible conditions is generally observed in the instantaneous images of these studies. Although the images of Clemens and Mungal do suggest a general increase in the size of the three-dimensional structures (end view) with increasing compressibility, the overall undulating nature of the mixing layer in this view renders comparisons rather difficult.

The quantification of the dominant, large-scale structural features for a given flow condition, as presented herein, can be utilized in several ways that may lead to better understanding of entrainment and scalar mixing. For instance, the measured structure sizes and orientations may be useful in providing a compressibility correction to the incompressible mixing layer entrainment model of Dimotakis.[26] To achieve this would require that additional correlations be made such that the ensemble-averaged spacing of the large structures was known. Furthermore, the angular orientation of the covariance fields of the transverse structures represents, on an ensemble-averaged basis, the direction of the main concentration gradient in a large structure (for the scalar transport seeded cases). With simple models, Clemens and Mungal[10] illustrated the influence that scalar ramps have on the scalar probability density functions (PDFs). Concentration gradients only in the streamwise direction (as originally proposed by Fiedler[27] for incompressible mixing) will yield a nonmarching PDF, whereas gradients in only the transverse direction will produce a marching PDF. Ramps in both directions will also produce marching PDFs. Marching PDFs in the compressible mixing layer have been reported by Dutton et al.,[28] Clemens and Mungal,[10] and Messersmith and Dutton.[22,23,29] For the present experiments, the covariance results suggest that the lower compressibility case will yield a more clearly defined marching PDF than the higher compressibility case, since the angular orientation and, subsequently, the degree of the transverse ramp of the ensemble-averaged large structure decrease with increasing compressibility.

V. Conclusions

It is known that large structures play an important role in the initial development of low-speed mixing layers, as well as being a key mechanism in entrainment, mixing, and the cascade of turbulent scales, yet the importance of large structures in compressible mixing layers is not fully understood. The present investigation has sought to identify and characterize, in an objective manner using statistical analysis of large image ensembles, the predominant features of large structures found in compressible mixing layers. The results of the two-dimensional spatial covariance field analysis are seen to agree with the predictions of linear stability theory and also to support the suggested trends concluded from visual interpretation of individual flow visualizations. More importantly, this investigation provides quantification of these trends that has at present not been established by either simulations or by other flow visualization studies.

The influence of compressibility, as quantified by the relative Mach number, was of primary interest. The study utilized imaging of the large structures by laser sheet Mie scattering techniques. Condensed ethanol droplets were used as the scattering media. Large ensembles of digital images were collected at three distinct flow conditions, $M_r = 0.63$, 0.98, and 1.49, and analyzed for the two-dimensional spatial covariance fields. A variety of mixing layer structures was observed within the ensembles for all three flow conditions. These structures included realizations of large, spanwise roller-type vortices as well as smaller, streamwise vortices.

The transverse image plane covariance fields suggest dominant structures characteristic of two-dimensional spanwise vorticity. The

structures are elliptical in shape and generally increase in size and have relatively constant eccentricity, whereas their angular orientation to the streamwise flow direction decreases, as the relative Mach number increases. Oblique image plane covariance fields indicate structures of smaller size and smaller eccentricity (i.e., more rounded) than their transverse counterparts. As seen in the oblique images, the three-dimensional influence of streamwise vorticity serves to reduce the elliptical correlation, hence the smaller, rounder structure shape. The relative size of the streamwise-oriented structures, with respect to the mixing layer thickness, generally increases with increasing relative Mach number, whereas their eccentricity decreases. Indeed, on a relative basis, the oblique structures grow more than the transverse structures as the relative Mach number increases. Thus, compressibility has a significant impact upon the growth of three-dimensional structures in mixing layers.

Acknowledgments

The authors wish to acknowledge the sponsorship of the Office of Naval Research (G. D. Roy) as well as the U.S. Air Force Wright Laboratories (A. S. Nejad). Additionally, cooperation and technical discussions with H. Krier, as well as the laboratory assistance provided by M. R. Gruber and T. Sonethongkham, are greatly appreciated.

References

[1]Bogdanoff, D. W., "Compressibility Effects in Turbulent Shear Layers," *AIAA Journal*, Vol. 21, No. 6, 1983, pp. 926, 927.

[2]Papamoschou, D., and Roshko, A., "The Compressible Turbulent Shear Layer: An Experimental Study," *Journal of Fluid Mechanics*, Vol. 197, Dec. 1988, pp. 453–477.

[3]Papamoschou, D., "Structure of the Compressible Turbulent Shear Layer," AIAA Paper 89-0126, Jan. 1989.

[4]Goebel, S. G., and Dutton, J. C., "Experimental Study of Compressible Turbulent Mixing Layers," *AIAA Journal*, Vol. 29, No. 4, 1991, pp. 538–546.

[5]Brown, G. L., and Roshko, A., "On Density Effects and Large Structure in Turbulent Mixing Layers," *Journal of Fluid Mechanics*, Vol. 64, July 1974, pp. 775–816.

[6]Goebel, S. G., "An Experimental Investigation of Compressible, Turbulent Mixing Layers," Ph.D. Thesis, UILU-ENG Rept. 90-4005, Dept. of Mechanical and Industrial Engineering, Univ. of Illinois, Urbana, IL, May 1990.

[7]Hall, J. L., Dimotakis, P. E., and Rosemann, H., "Experiments in Non-Reacting Compressible Shear Layers," AIAA Paper 91-0629, Jan. 1991.

[8]Clemens, N. T., "An Experimental Investigation of Scalar Mixing in Supersonic Turbulent Shear Layers," Ph.D. Thesis, HTGL Rept. T-274, Mechanical Engineering Dept., Stanford Univ., Stanford, CA, May 1991.

[9]Clemens, N. T., and Mungal, M. G., "Two- and Three-Dimensional Effects in the Supersonic Mixing Layer," *AIAA Journal*, Vol. 30, No. 4, 1992, pp. 973–981.

[10]Clemens, N. T., and Mungal, M. G., "Large-Scale Structure and Entrainment in the Supersonic Mixing Layer," *Journal of Fluid Mechanics*, Vol. 284, Feb. 1995, pp. 171–216.

[11]Elliott, G. S., Samimy, M., and Arnette, S. A., "A Study of Compressible Mixing Layers Using Filtered Rayleigh Scattering," AIAA Paper 92-0175, Jan. 1992.

[12]Messersmith, N. L., Dutton, J. C., and Krier, H., "Experimental Investigation of Large Scale Structures in Compressible Mixing Layers," AIAA Paper 91-0244, Jan. 1991.

[13]Messersmith, N. L., "An Experimental Investigation of Organized Structure and Scalar Mixing in Compressible Turbulent Free Shear Layers," Ph.D. Thesis, UILU-ENG Rept. 92-4002, Dept. of Mechanical and Industrial Engineering, Univ. of Illinois, Urbana, IL, Jan. 1992.

[14]Clemens, N. T., and Mungal, M. G., "A Planar Mie Scattering Technique for Visualizing Supersonic Mixing Layers," *Experiments in Fluids*, Vol. 11, No. 2/3, 1991, pp. 175–185.

[15]Samimy, M., Reeder, M. F., and Elliott, G. S., "Compressibility Effects on Large Structures in Free Shear Flows," *Physics of Fluids A*, Vol. 4, No. 6, 1992, pp. 1251–1258.

[16]Sandham, N. D., and Reynolds, W. C., "Compressible Mixing Layer: Linear Theory and Direct Simulation," *AIAA Journal*, Vol. 28, No. 4, 1990, pp. 618–624.

[17]Sandham, N. D., and Reynolds, W. C., "Three-Dimensional Simulations of Large Eddies in the Compressible Mixing Layer," *Journal of Fluid Mechanics*, Vol. 224, March 1991, pp. 133–158.

[18]Soetrisno, M., Greenough, J. A., Eberhardt, D. S., and Riley, J. J., "Confined Compressible Mixing Layers: Part I. Three-Dimensional Instabilities," AIAA Paper 89-1810, June 1989.

[19]Soetrisno, M., "Numerical Simulations of Instabilities in Compressible Mixing Layers," Ph.D. Thesis, Dept. of Aeronautics and Astronautics, Univ. of Washington, Seattle, WA, 1990.

[20]Gruber, M. R., Messersmith, N. L., and Dutton, J. C., "The Three-Dimensional Velocity Field in a Compressible Mixing Layer," *AIAA Journal*, Vol. 31, No. 11, 1993, pp. 2061–2067.

[21]Bernal, L. P., and Roshko, A., "Streamwise Vortex Structure in Plane Mixing Layers," *Journal of Fluid Mechanics*, Vol. 170, Sept. 1986, pp. 499–525.

[22]Messersmith, N. L., and Dutton, J. C., "Mie Scattering and Laser-Induced Fluorescence Measurements of Scalar Mixing in Compressible Free Shear Layers," *Laser Techniques and Applications in Fluid Mechanics VI*, edited by R. J. Adrian, D. F. G. Durão, F. Durst, M. V. Heitor, M. Maeda, and J. H. Whitelaw, Springer–Verlag, Berlin, 1993, pp. 415–432.

[23]Messersmith, N. L., and Dutton, J. C., "Mie Scattering Measurements of Probability Density Functions in Compressible Mixing Layers," *Experiments in Fluids* (to be published).

[24]Long, M. B., Chu, B. T., and Chang, R. K., "Instantaneous Two-Dimensional Gas Concentration Measurements by Light Scattering," *AIAA Journal*, Vol. 19, No. 9, 1981, pp. 1151–1157.

[25]Bendat, J. S., and Piersol, A. G., *Random Data: Analysis and Measurement Procedures*, 2nd ed., Wiley, New York, 1986.

[26]Dimotakis, P. E., "Two-Dimensional Shear Layer Entrainment," *AIAA Journal*, Vol. 24, No. 11, 1986, pp. 1791–1796.

[27]Fiedler, H. E., "Transport of Heat Across a Plane Turbulent Mixing Layer," *Advances in Geophysics*, Vol. 18A, 1974, pp. 93–109.

[28]Dutton, J. C., Burr, R. F., Goebel, S. G., and Messersmith, N. L., "Compressibility and Mixing in Turbulent Free Shear Layers," *12th Symposium on Turbulence*, Dept. of Chemical Engineering, Univ. of Missouri–Rolla, MO, Sept. 1990.

[29]Messersmith, N. L., and Dutton, J. C., "Laser-Induced Fluorescence Measurements of Scalar Transport in Compressible Mixing Layers," AIAA Paper 92-3547, July 1992.